Pergamon

Optimization of Phosphorus Localization by EFTEM of Nucleic Acid Containing Structures

C. QUINTANA*¶, S. MARCO†, N. BONNET‡, C. RISCO†, M.L. GUTIÉRREZ§, A. GUERRERO§ and J.L. CARRASCOSA†

*Instituto de Microelectrónica de Madrid, CNM-CSIC, Parque tecnológico de Madrid, Isaac Newton 8, E-28760 Madrid, Spain
†Centro Nacional de Biotecnología, CSIC, Campus Universidad Autónoma, Cantoblanco, E-28049 Madrid, Spain
‡INSERM Unit 314 and Université de Reims (LERI), 21 rue Clément Ader, F-51685 Reims Cedex, France
§Departamento de Electrónica, Facultad de Físicas, Universidad Complutense de Madrid, 28040 Madrid, Spain

Abstract—Energy Filtered Transmission Electron Microscopy (EFTEM) has been used to study nucleic acids localization in unstained thin sections of virus-infected cells. For this purpose, phosphorus maps (P-maps) have been obtained by applying the N-windows Egerton model for background subtraction from data acquired by a non-dedicated TEM Jeol 1200EXII equipped with a post-column PEELS Gatan 666-9000 and a Gatan Image Filter (GIF-100). To prevent possible errors in the evaluation of elemental maps and thus incorrect nucleic acid localization, we have studied different regions of swine testis (ST) cells with similar local density containing either high concentration of nucleic acids (condensed chromatin and ribosomes) or a very low concentration (mitochondria). Special care was taken to optimize the sample preparation conditions to avoid as much as possible the traditional artifacts derived from this source. Selection of the best set of pre-edge images for background fitting was also considered in order to produce "true P-maps". A new software for interactive processing of images series has been applied to estimate this set. Multivariate Statistical Analysis was used as a filtering tool to separate the "useful information" present in the inelastic image series (characteristic signal) from the "non-useful information" (noise and acquisition artifacts). The reconstitution of the original image series preserving mainly the useful information allowed the computation of P-maps with improved signal-to-noise ratio (SNR). This methodology has been applied to study the RNA content of maturation intermediate coronavirus particles found inside infected cells. © 1998 Elsevier Science Ltd. All rights reserved.

Key words: EFTEM, elemental P-maps, image processing, coronaviruses.

INTRODUCTION

The localization of chemically defined components in ultrathin sections of biological material has been a central subject of interest in structural biology for many years. In particular, the role of phosphorus as a position marker of nucleic acids is a topic that has deserved considerable effort (Ottensmeyer and Andrew, 1980; Bazett-Jones and Ottensmeyer, 1981; Adamson-Sharpe and Ottensmeyer, 1981; Korn et al., 1983; Harauz and Ottensmeyer, 1984; Ottensmeyer et al., 1988; Rattner and Bazett-Jones, 1989; Heng et al., 1990; Özel et al., 1990; Bazett-Jones, 1993; Harauz et al., 1995; Abolhassani-Dadras et al., 1994, 1996; Olins et al., 1996; Vazquez-Nin et al., 1996; Beniac et al., 1997a, b).

We are interested in the study of viral morphogenesis and, especially, in the incorporation of the nucleic acid into the morphogenetic intermediates. There are several classical approaches to this problem, such as cytochemical methods and in situ hybridization. Nevertheless, these methodologies have low efficiency and sensitivity for RNA localization. Direct observation of nucleic acids with higher efficiency in ultrathin sections of virus-infected cells is thus a challenging objective that could be reached using in situ spectroscopic methods by the analysis of the P distribution, based

on the specific elemental concentration of phosphorus in nucleic acids (around 3 at.%).

Phosphorus-maps (P-maps) in cellular nuclei components can be obtained by X-ray spectroscopy as reported, for example, by Le Furgey et al. (1992) using cryofixed and cryodehydrated frozen sections, and by Quintana and Bonnet (1994a,b) using cryofixed, cryosubstituted and cryoembedded sections. In these cases the main drawback is the long acquisition time required to produce a data set (from one to several hours). Electron Energy Loss Spectroscopy (EELS) possesses higher sensitivity and spatial resolution than X-ray microanalysis for light elements (Leapman and Hunt, 1991; Krivanek et al., 1992). It has been used to obtain P-maps of nucleic acid (n.a.)-containing structures since 1980 (Ottensmeyer and Andrew, 1980). Recent implementation of commercially available in-column and post-column electron energy loss spectrometers has increased the use of energy-filtered transmission electron microscopy (EFTEM), with special emphasis on chemical mapping.

One of the main problems when dealing with elemental map computation in EFTEM is the subtraction of a non-negligible background that lies under the characteristic elemental signal. This is especially important in the case of elements being present at a very low concentration, where the absolute value of the characteristic signal is much smaller than the background. The choice of the best
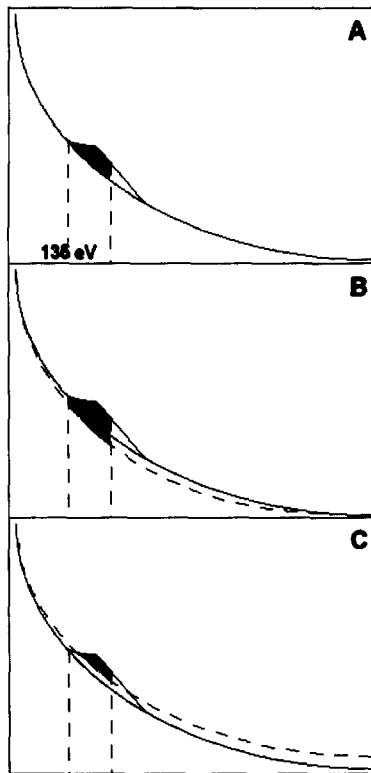
Fig. 1. The EELS background subtraction problem. A) Correct background subtraction. The elemental map is a "true map". B) Bad background subtraction. The calculated curve (discontinuous line) is below the correct background curve (continuous line). Thus, the elemental map (black area) is overestimated and includes part of the mass-thickness. C) Bad background subtraction. The calculated curve (discontinuous line) is over the correct background curve (continuous line), leading to a underestimation of the elemental map (black area).

background subtraction method therefore becomes critical. Background subtraction problems in EFTEM can be summarized as shown in Fig. 1. Case (a) represents background subtraction from a model that is correctly fitted to the pre-edge images. In contrast, cases (b) and (c) represent incorrect adjustments that will render incorrect maps. Case (b) gives rise to overestimation of the elemental map (this includes the characteristic signal and part of the background), and case (c) leads to underestimation of the elemental map.

Among the different methods currently accepted for map extraction, one of the most widely used models the background by the power law, $B = A \times E^{-R}$ (Egerton, 1975). This method involves the computation of two parameters (A and R) and is also known as the "three-window" method, as it requires the acquisition of three images, two below the characteristic energy loss edge of the element (pre-edge images) and one above this energy loss value (post-edge image). It has been subsequently extended to N pre-edge and M post-edge images (Jeanguillaume *et al.*, 1978; Bonnet *et al.*, 1988). Other mathematical formulae have been also used to model the background (Ottensmeyer, 1986; Bonnet *et al.*, 1988; Ottensmeyer and Frankland, 1988; Tenailleau and Martin, 1992). Negative results obtained in the case of P detection in mitochondrial dense granules originated from rat cultivated chondrocytes (Trebbia and Mory, 1990), however, suggested that in the

case of P-maps in biological sections, the power law is not valid in the region of the pre-edge images in the $L_{2,3}$ transition in P (100 to 135 eV), due to the tail of the very intense "plasmon peak". The plasmon influence is even more important if the sample possesses a high mass-thickness (high thickness and/or high density in stained samples). This situation is similar to that shown in Fig. 1(c), in which P-maps could be under-estimated.

For this reason, some authors continue to use another approach for background subtraction that is based on the acquisition of only two images (two-window methods): (1) The scaled subtraction of one pre-edge image from the post-edge one (Ottensmeyer and Andrew, 1980; Korn *et al.*, 1983). (2) The ratio between the post and the pre-edge images (also known as the jump method), used mainly in Material Science to avoid crystal diffraction effects (Krivanek *et al.*, 1992; Hofer *et al.*, 1995). Both methods increase the signal-to-noise ratio (SNR) of the maps, and they are presently used for this reason (Olins *et al.*, 1996, Beniac *et al.*, 1997a, b). In spite of rendering a good SNR, scaled two-window methods may produce false positive signals in high density areas, irrespective of the presence of P (Leapman, 1986). This is particularly relevant in preparations treated with heavy metal salts (osmium, uranium or lead). In this case, the computed maps can be considered a mixture of density and elemental P-map, not allowing separation of both signals (Bonnet *et al.*, 1988; Bonnet, 1995), a case similar to that shown in Fig. 1b.

Cellular components P-maps have been a good test for background subtraction methods, as phosphorus represents less than 0.5% in mass concentration in these biological samples. By means of the spectrum-image acquisition technique in an STEM, reliable P-maps with good SNR were built of DNA in the head of a bacteriophage (Shuman *et al.*, 1986, Colliex *et al.*, 1994) using a three-window method for background subtraction. This technique requires, however, long acquisition time (around 22 minutes for 32x64 pixel images (Shuman *et al.*, 1986) or 20 minutes for 64x64 pixel images (Colliex *et al.*, 1994). More recently, using a TEM equipped with an in-column spectrometer, it has been possible to obtain P-maps of nucleic acid-containing structures with a high SNR by applying the three-window method (Vazquez-Nin *et al.*, 1996). Electron spectroscopic imaging of sectioned viruses has provided high-contrast imaging and an improvement of the resolution of the viral particles, also allowing a better detectability of the immunolabeling markers (Özel *et al.*, 1990). Also, P-maps were obtained using a two-window method to study the organization of encapsidated DNA in vaccinia virus (Harauz *et al.*, 1995). Interpretation problems arose in this case due to the fact that the samples were conventionally fixed and embedded.

In a previous study, our post-column PEELS and Image Filter (IF) was characterized and reliable Fe-maps were produced from images acquired in a few seconds (Quintana *et al.*, 1997). Using this set-up, we have studied P-map computation using very thin unstained sections of cryosubstituted and HM23 resin cryoembedded swine testis (ST) cells, infected with a coronavirus. After checking the background subtraction method to separate the P-signal from mass-thickness contribution, we have applied Multivariate

Statistical Analysis and, in particular, Factorial Analysis of Correspondence (FAC) (Bonnet et al., 1988; Bonnet et al., 1992; Bonnet and Trebbia, 1992; Trebbia and Mory, 1990; Bonnet, 1995) to the series of pre- and post-$L_{2,3}$ P-edge images. Such factorial filtering allows noise reduction and elimination of artifacts that might have been produced in image acquisition and thus enables presentation of clearer and more reliable images of the P-containing structures. Once the methods were tested using cellular components of known elemental composition, we studied the RNA distribution of intracellular coronavirus particles.

MATERIAL AND METHODS

Sample preparation

Monolayers of ST cells infected with the transmissible gastroenteritis coronavirus (TGEV) were produced as described in Risco et al. (1995). After collection, cells were fixed in situ with a mixture of 2% glutaraldehyde and 2% tannic acid in 0.4 M HEPES buffer (pH 7.5), for 1 h at room temperature. Fixed monolayers were removed from the dishes in the fixative and transferred to Eppendorf tubes. After centrifugation in a microcentrifuge and washing with HEPES buffer, small pellets of fixed cells were cryo-protected with glycerol and applied to 1 mm^2 pieces of filter paper, blotted with filter paper for 15 s, and quickly frozen in home-made equipment (Quintana, 1991) using commercial liquid propane cooled by liquid nitrogen at −196°C. Vitrified specimens were stored in liquid nitrogen until use. For freeze-substitution, samples were transferred to a Reichert Jung (Leica, Austria) AFS freeze-substitution unit, and maintained 24 h at −90°C in pure methanol for complete substitution of the water in the sample, according to established procedures (Grief et al., 1994; Quintana, 1994). Samples were then processed for cryoembedding in Lowicryl HM23 at −60°C. Polymerization was done with ultraviolet light for 24 h at −60°C and a further 12 h at room temperature. Ultra-thin (20–30 nm) sections were mounted on uncoated 400-mesh copper grids. Some sections were coated with a thin layer of carbon to increase the stability against the electron radiation.

Instruments

The microscope used was a TEM Jeol 1200EX II with a conventional tungsten gun. The microscope is equipped with a Gatan anti-contaminator model 651N and a ± 60° tilting goniometer. The optical characteristics of this configuration are: focal length = 5 mm, Cc = 3.9 mm, and Cs = 5.6 mm. The microscope is operated at 120 kV. This instrument has been equipped with a PEELS Gatan 666-9000 and a Gatan Image Filter (GIF-100) (Krivanek et al., 1995a).

Experimental conditions

Unfiltered bright field images, Z-loss images and inelastic filtered images of 512 × 512 pixels were recorded using the slow-scan CCD and the Gatan Digital Micrograph software

working at 16 bits. The experimental conditions were:. emission current = 7–8 μA. condenser aperture = 300 μm. semi-illumination angle = 2 mrad. objective aperture = 40 μm. acceptance half-angle = 4 mrad. semi-collection angle = 4.5 mrad. aperture entrance of the spectrometer = 3 mm.. spot size = 1; defocused mode in unfiltered or Z-loss images, focused mode in filtered images (minimun diameter of the iluminated area = 2 μm)

All digital images were corrected for dark current and gain variations of the SS-CCD camera using Digital Micrograph software.

The microscope magnification ranged from 600 to 3000x. Taking into account the image magnification due to the GIF optical system (20X), the total magnification varied from 12 000 (2 nm /pixel) to 60 000 (0.4 nm/pixel). The acquisition time was 0.5 s for unfiltered and Z-loss images and 3 to 4 s for energy-filtered images.

P-maps can be obtained using two characteristic inner shell ionization edges, the $L_{2,3}$ at 135 eV and the K at 2149 eV. Although the K ionization edge has a better signal:background ratio (SBR) than the $L_{2,3}$ edge, it has lower intensity. We have thus chosen the $L_{2,3}$ edge, in spite of its smaller SBR.

Energy-filtered images were recorded below and above the ionization edge $L_{2,3}$ of P from 95 to 155 eV with a $\delta E =$ 10 eV energy window slit. The energy losses of these images were selected by raising the high voltage of the microscope. This procedure ensures no change in image focusing. Due to differences in optimum focus between inelastic images and bright field images, inelastic images were acquired with a focus adjusted after the ionization edge, around 145 eV, by using a real-time CCD camera.

Computer analysis of the series of inelastic images

Preprocessing

Inelastic images belonging to each series were drift-corrected by cross-correlation algorithms. Only the common area from all images in each series was considered for processing. A median filter (neighborhood: 3 × 3 pixels) was applied to the images (Bonnet et al., 1988).

Map extraction

Background subtraction

We have used the extension of the three-window method applied to N pre-images and M post-images (Jeanguillaume et al., 1978; Bonnet et al., 1988). This method (Egerton, 1975) involves the fitting of the following expression

$$B = A \times E^{-R}$$

to the background below the edge of interest (E is the energy loss and A and R the fitting parameters that are computed, pixel by pixel, from two or more pre-edge images). The background image under the post-edge image is then computed by extrapolation and the characteristic signal is extracted by subtraction.

We have used a program developed for the analysis of image sequences, whatever their origin (Bonnet and Zahm,
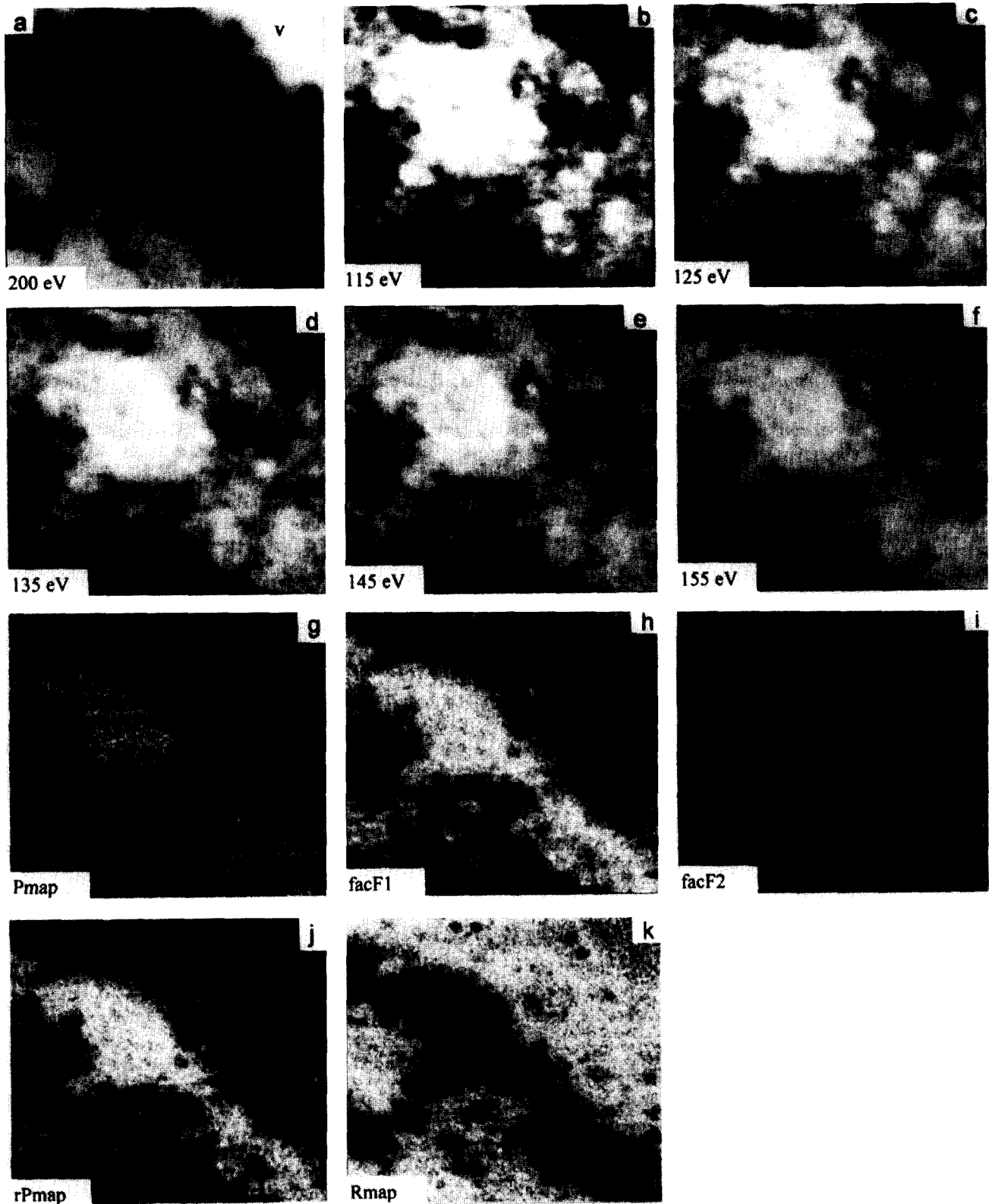
Fig. 2. Low magnification series (12 000 ×) containing part of one cell and embedding resin. A) Structure-sensitive contrast image acquired at an energy loss about 200 eV. Labeling shows the TGEV viral particles (v), cytoplasm (cyt) and condensed chromatin (chr). b) to f) Inelastic images obtained at 115, 125, 135, 145 and 155 eV, respectively. g) P-map obtained using 115, 125 and 135 eV as pre-edge images, and 145 and 155 eV as post-edge images. h) Coordinates of the pixels over factorial axis 1 after conversion to "gray levels", (F1). i) Factorial image over axis 2. j) P-map obtained using 115, 125 and 135 eV as pre-edge images, and 145 and 155 eV as post-edge images, after reconstitution with factorial axes 0 and 1. k) R-map obtained from reconstituted images. Bar represents 300 nm.

1998). Our version (for 16-bit images) runs on a SUN workstation, and allows:

a) visualization of the whole image series

b) interactive selection of regions of interest (ROIs)

c) display of the signal (inelastic transmitted intensity), integrated within a defined ROI, as a function of the energy loss

d) determination of the best background extrapolation and

background subtraction, to compute characteristic maps using several background models.

Image series factorial analysis of correspondence (FAC)

FAC belongs to Multivariate Statistical Analysis (MSA), a group of methods devised to analyse information from the whole data set at once. FAC can be used to discard redundant information and to display graphically correlation and anti-correlation among different images of the series, as well as for the correlation and anti-correlation among image pixels, without an explicit model of the data. The only implicit assumption in this approach is to consider the whole data set as a linear combination of several underlying components (factorial axes).

MSA can be applied hierarchically to classify the information contained in the data set. In the case of a series of inelastic images acquired below and above a characteristic edge, the information corresponds to:

- the characteristic signal
- the background
- the noise and the acquisition artifacts

If, as a consequence of the analysis, it is possible to identify some of the underlying components as "useful", it is then possible to reconstitute the data set using only such information, therefore filtering the rest of the information. In that sense, components not considered would correspond to noise and acquisition artifacts and would be removed (Bonnet et al., 1988; Trebbia and Bonnet, 1990; Trebbia and Mory, 1990; Bonnet et al., 1992; Bonnet and Trebbia, 1992; Bonnet, 1995).

Software applied was developed in a version for 16-bit images that runs on a SUN workstation.

Final data handling and presentation

After data treatment, the histograms of images and maps were centred (average ± 3 × standard deviation) and final computed images at 8 bits were transferred in an LZW compression TIFF format to a PC, to be printed using a high-resolution graphic card. As this representation did not allow visualization of the contrast changes among the different series images, we have represented the first series of images using the variance of the 155 eV image as an standard for all the images. Final hard copies were obtained in a Laser Printer HP4M with a resolution of 3200 dpi.

RESULTS

P-maps on test objets

Two different series of inelastic filtered images of ultra-thin unstained sections of ST cells infected with TGEV coronavirus were used to test the background subtraction method:

a) Low magnification series (12 000 ×), containing part of a cell and embedding resin. Images show (Fig. 2) part of the nucleus with peripheral condensed chromatin (chr), the cytoplasm (cyt) containing some ribosomes and a few

extracellular viruses (v) attached to the plasma membrane of the cell. In this series, structures containing higher concentration of n.a. (chromatin, ribosomes and viruses) correlate with regions of higher local density.

b) Intermediate magnification series (24 000 ×) of ST cells (Fig. 3) containing cytoplasm (cyt), one mitochondrion (mit) and ribosomes in the rough endoplasmic reticulum (rer). In this series, the mitochondrion, with a very low n.a. content, has a similar local density to the ribosomes in the rer.

Structural data were extracted from the inelastic dark-field-like images acquired at an energy loss of approximately 200 eV, which correspond to the structure-sensitive contrast images (Reimer and Messemer, 1990). In these images (Fig. 2a and Fig. 3a), the darker regions are of higher mass thickness. For P-map computation, inelastic images were acquired before and after the $L_{2,3}$ P characteristic edge at 135 eV. Representative images of the series are shown in Fig. 2b–f and Fig. 3b–f.

Using the software described in Materials and Methods, different ROIs were selected, including condensed chromatin, (circular region of 25 pixels radius), resin (circular region of 25 pixels radius), rer ribosomes (9 circular regions of 5 pixels radius each) and mitochondria (circular region of 45 pixels radius). After displaying the signal as a function of energy loss within every ROI and applying the Egerton power law to the different subsets of pre-edge images, the A, R and χ^2 parameters were computed in each case. Fit quality was estimated by the χ^2 value normalized to the number (N) of pre-edge images used. Results of some regions are shown in Table 1.

The best fit was obtained for the subset composed of images at energy loss values of 115, 125 and 135 eV in series 1 (Fig. 2b, c, d) and of images with energy loss values of 105, 125 and 135 eV in series 2 (Fig. 3b, c, d).

Plots shown in Fig. 4a correspond to the set of pre-edge images of series 1 that produced the best fit (in chromatin and resin), together with the estimated background extrapolated beyond the characteristic energy loss edge. Fig. 4b presents the image set for series 2 in the case of rer and mitochondria. In both cases, in ROIs corresponding to structures containing a high n.a. concentration (chromatin and the rer ribosomes), the 145 eV and 155 eV post-edge images possess values well above the background curve, indicating the presence of phosphorus. In the case of ROIs with a low n.a. content (mitochondria), or without n.a. (resin), these values are close to the background curve. This is better observed in Fig. 4c, which plots the net intensity after background substraction, showing much higher values for chromatin than for resin in the post-edge images of series 1.

P-maps computed using the N-windows method with three pre-edge images and two post-edge images are shown in Fig. 2g and 3h. Cellular structures known to contain high n.a. levels exhibit strong signals in the P-maps (notice, for example, the chromatin and virions in Fig. 2g and the ribosomes of rer cisternae in Fig. 3h, while some other cellular structures of similar local density known to contain low n.a. levels, totally disappear in the P-maps (mitochondrion in Fig. 3h, for example).
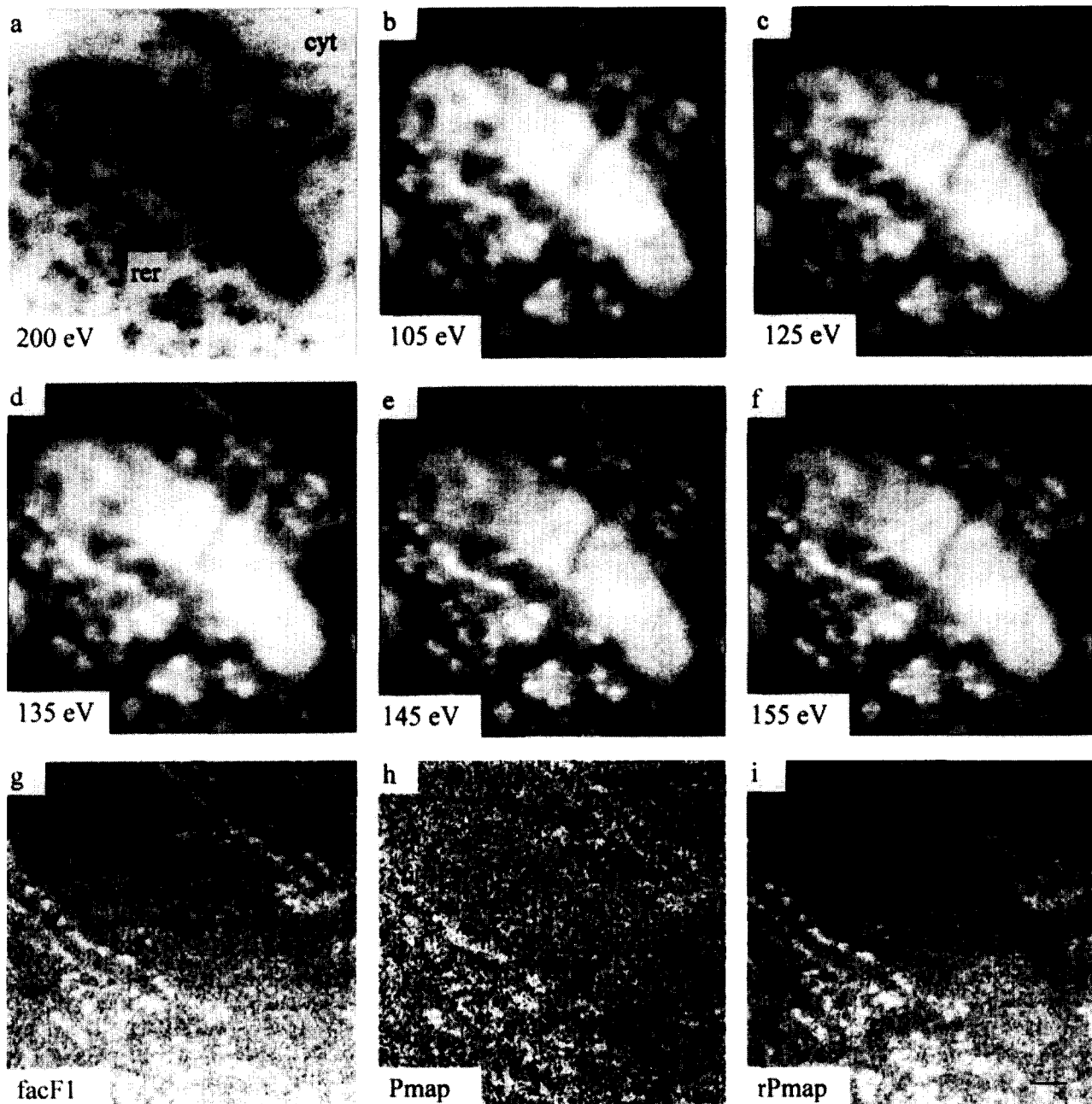
Fig. 3. Intermediate magnification series (24 000 ×) of ST cells. a) Structure-sensitive contrast image acquired at an energy loss of about 200 eV. Labeling shows the mitochondria (mit), cytoplasm (cyt) and rough endoplasmic reticulum (rer). b) to f) Inelastic images obtained at 105, 125, 135, 145 and 155 eV, respectively. g) Coordinates of the pixels over factorial axis 1 (F1). h) P-map obtained using 105, 125 and 135 eV as pre-edge images and 145 and 155 eV as post-edge images. i) P-map obtained using images 105, 125 and 135 eV as pre-edge images, and 145 and 155 eV as post-edge images after reconstitution with factorial axes 0 and 1. Bar represents 100 nm.

Factorial filtering

FAC has been applied to a set of pre- and post-edge images previously selected as described above for each case. The contribution of each factorial axis to the total variance is shown in Table 2.

Image and image pixel coordinates over factorial axis were computed. Fig. 5 shows image coordinates of series 1 on axis 1 vs. energy loss. Pixel coordinates over factorial axis, after conversion to "gray levels", can be mapped and displayed as "factorial images". Factorial images allowed visualization of the different sources of information in the original data set. Factorial images (F1 and F2) of series 1 are

shown in Fig. 2h and i, while the first factorial image of series 2 is shown in Fig. 3g.

From the energy loss point of view, axis 1 (about 70% of the total variance) shows that the post-edge images correlate well among them and anti-correlate with the pre-edge images. Regarding the subcellular compartments, axis 1 differentiates nucleic acid-containing structures from the rest of the areas. Factorial images from axis 2 and 3 only presented noise (see Fig. 2i which represents factorial image from axis 2, from series 1).

Image series were finally reconstituted using the information contained in the factorial axes 1 and 0 (the factorial axis 0 carrying the information of the average image computed
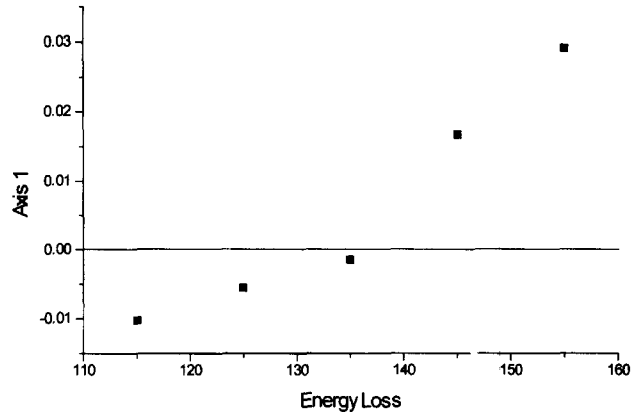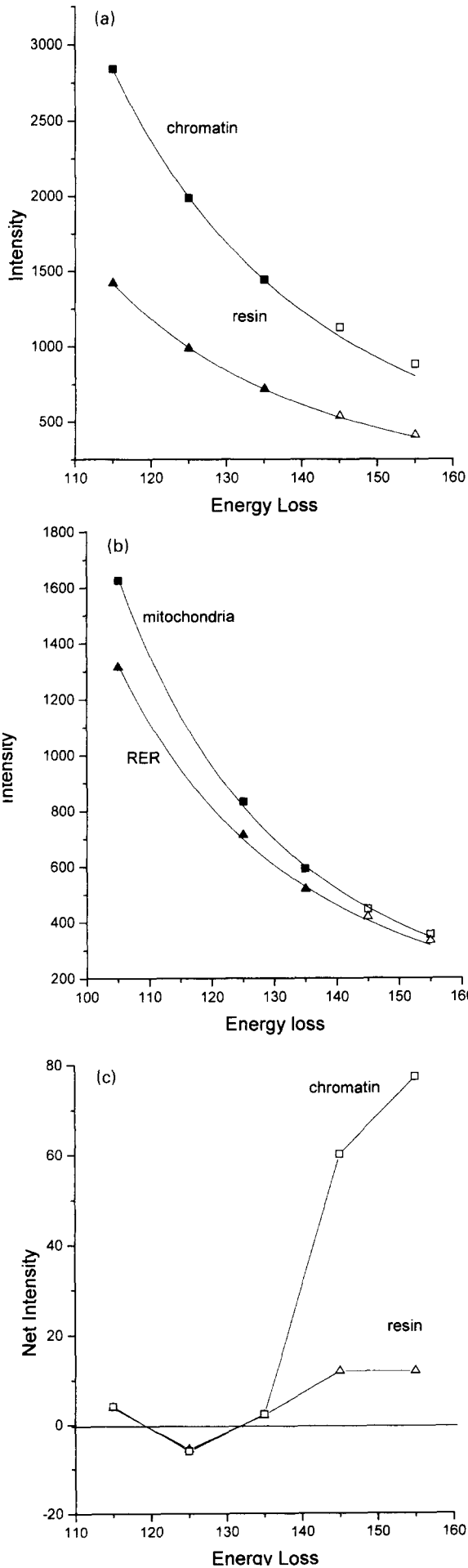
Fig. 5. Coordinates of images of series 1 over factorial axis 1 versus their energy loss values. Note that axis 1 allows clear discrimination between pre- and post-edge images. Axis 1 represents 67.9% from the total variance.

from the original data set after normalization). We have verified that this reconstitution does not cause any undesirable effects in the estimation of the background model, as it does not modify either the average and standard deviation values of the images or the average values of the R-map obtained from the pre-edge images (Table 3). The reconstituted R-map from series 1 is shown in Fig. 2k. P-maps obtained with reconstituted images are shown in Fig. 2j and Fig. 3i. The enhancement of the signal-to-noise ratio of these maps with respect of the original ones (Fig. 2g and Fig. 3h) is clearly observed and allows the definition of the boundaries of the different structural elements that are obscured in the original images.

Study of the P distribution of intracellular virions

The methods described above were applied to series of inelastic images of intracellular virions. Z-loss and structure-sensitive contrast images of a group of virions are shown in Fig. 6a and b respectively. In these images, TGEV viral particles with two different sizes are visible. Their internal structure is indistinguishable in the Z-loss image, while some hints of internal differences appeared in the structure-sensitive contrast image. No significant difference was observed in the χ^2/N value as a function of the pre-edge image number (3, 4 or 5) considered when fitting the background (Table 1).

Plots presented in Fig. 7 correspond to the power law fit of background over 5 pre-edge images in 2 ROIs, corresponding to viruses and cytoplasm. As in the previous test series, images obtained at 145 and 155 eV (Fig. 6f and g, respectively) showed values above the extrapolated background curve in virus regions, thus indicating the presence

Fig. 4. Plots of average counts versus energy loss values in different regions of interest (ROIs). Continuous line represents the adjusted Egerton Power Law background curve using the pre-edge images (before 145 eV). a) Data in chromatin and resin (series 1). Note that values at 145 and 155 eV in chromatin are over the background curve, indicating the presence of P. b) Data in rer and mitochondria (series 2). Values at 145 and 155 eV in rer are over the background curve, indicating the presence of P. c) Net intensity versus energy loss for chromatin and resin in series 1.

Table 1. Estimation of A, R and normalized χ^2/N values using different numbers, N, of pre-edge images between 85 and 135 eV

Pre-edge images	Series 1			Series 2			Series 3		
Number (N)	A	R	χ^2/N	A	R	χ^2/N	A	R	χ^2/N
6				3.7×10^{11}	4.13	2.0			
5	4.9×10^{10}	3.52	4.87	3.1×10^{11}	4.09	0.38	1.0×10^{11}	4.37	0.055
4	8.3×10^{10}	3.63	5.67	2.5×10^{11}	4.05	0.28	9.4×10^{10}	4.34	0.055
3	1.6×10^{11}	4.24	1.5×10^{-3}	1.8×10^{11}	3.98	0.18	2.2×10^{11}	4.53	0.061

Table 2. Percentage of variance values for each factorial axis in series 1, 2 and 3

Axis	Variance series 1 (%)	Variance series 2 (%)	Variance series 3 (%)
1	67.92	69.90	20.2
2	14.03	17.50	17.5
3	9.29	12.50	16.7
4	8.76	0.0002	16.1
5			15.1

Table 3. Statistics of original and reconstituted images

Images (eV)	Mean	σ
115	2525	339
r115	2525	337
1215	1753	237
r125	1752	237
135	1264	173
r135	1264	173
145	959	139
r145	958	139
155	735	112
r155	734	112
Rmap	4.31	0.11
rRmap	4.32	0.05

of P. In ROIs selected within cytoplasm, corresponding values are essentially within the background curve, suggesting absence of P. The P-map obtained with 5 pre-edge images and 2 post-edge images is shown in Fig. 6h.

FAC was applied to all seven images used to obtain the P-map. In Table 2, the percentages of variance of the first five factorial axes can be seen. Images of this series were reconstituted with the information contained on factorial axes 0, 1 and 2. The resulting P-map (Fig. 6i) presents a clear enhancement of the SNR when compared to the first one obtained (Fig. 6h). These P-maps show that the large virions have a peripheral phosphorus signal distribution (as the central region seems devoid of P-signal), while the small virions present a more homogeneous internal distribution of the P-signal.

DISCUSSION

We have studied the possibility of obtaining true P-maps of biological samples, trying to avoid false P-signals due mainly to high density structures on one side and loss of true P-signals on the other, which would lead to missing out of important information. To this end, we have tested different well-characterized samples that have allowed us to make a qualitative assessment of processing methods used to build P-maps.

The main problem when obtaining low concentration

elemental maps by EELS is the very low SBR. It is therefore critical to optimize sample preparation conditions as well as data acquisition for a specific instrument to increase the SBR. As background intensity depends on mass-thickness, a reduction of section thickness, together with the use of low density embedding media, would lead to background intensity reduction. To this end, we have used ultra-thin sections (30 nm) and Lowicryl HM23 as embedding medium (density near one) in our studies.

The specific elemental signal can be increased by:

a) the optimization of the acquisition parameters
b) increasing the acquisition time (limited by the radiation damage tolerance of the sample)
c) optimizing the model applied to the background subtraction
d) decreasing noise and acquisition artifacts

Regarding acquisition parameter optimization, (Krivaneket *et al.*, 1995b) we have used the conditions for the best spatial resolution attainable by our instrument, as described previously (Quintana *et al.*, 1997). The acquisition time was adjusted as a compromise among the SNR, the radiation damage and the mechanical and magnetic stability of the sample and the instrument. Once these parameters were fixed, we concentrated our effort on points c and d.

The presence of drifts is usual in instruments not fully dedicated to microanalysis, due to environmental, mechanical and magnetic perturbations, as it is in our case. As a consequence, the energy loss values at which the images are acquired do not always correspond to the real ones. It is then very useful to be able to select, from among the pre-edge images of a series, those which best fit the model of the background to compute the P-maps. Best fit was chosen by means of the minimum χ^2/N criteria. For instance, in the second series we did not consider the image at 115 eV, and in the third series it was possible to detect that the image at 125 eV was slightly outside of the estimated background curve (Fig. 7). Another consequence of the presence of drift is the need to centre the images before their processing, a procedure that we perform by cross-correlation.

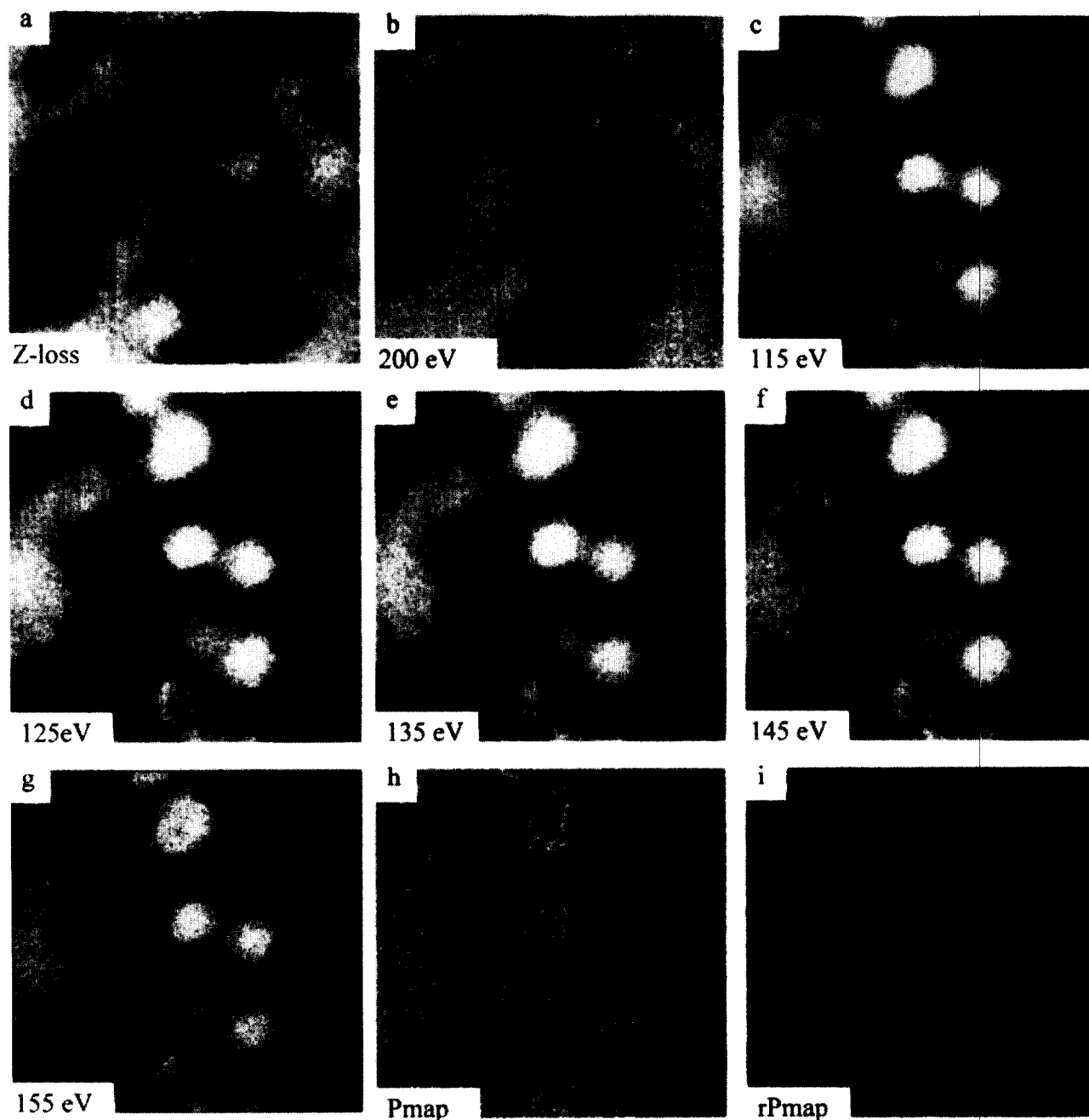The possibility of using more than one post-edge image

Fig. 6. Series corresponding to ultrathin sections of TGEV viral particles (60 000×). a) Z-loss image. b) Structure-sensitive contrast image acquired at an energy loss of about 200 eV. c) to g) Inelastic images obtained at 115, 125, 135, 145 and 155 eV. h) P-map obtained using images 95, 105, 115, 125 and 135 eV as pre-edge images and 145 and 155 eV as post-edge images. i) P-map using images 95, 105, 115, 125 and 135 eV as pre-edge images and 145 and 155 eV as post-edge images after reconstitution with factorial axes 0, 1 and 2. Two types of viral particles are seen: small particles (double arrows) and larger ones (arrow). Bar represents 100 nm.

increases the characteristic signal value and consequently the SNR of the maps. In our case, we have only used two post-edge images because of the proximity of the $L_{2,3}$ edge of the sulphur at 165 eV.

To test the background model, two different test series were used. In the first, the P-map obtained by applying the N-window method to three pre-edge and two post edge-images showed the presence of a clear positive P-signal in areas that contained nucleic acids, although the values for resin are not null (Fig. 4c). However, the areas with high P-signal correlate with areas of high "natural" local density in the sample, so the possibility could not be completely excluded that the signal might be a mixture of characteristic signal and mass-thickness (see model b in Fig. 1).

We performed a second test series in which, together with the structures containing high n.a. concentrations (ribosomes in the rer), there was an organelle with high local density (mitochondria) and very low concentrations of n.a. Curves for background fitting in the analysed ROIs (mitochondria and rer) and the P-map (obtained using three pre-edge images and two post-edge images) showed that there was only P-signal in the ribosomes and not in the mitochondria.

This methodology yields true P-maps which, nevertheless, possess a low SNR. Using factorial filtering of inelastic images, SNR of P-maps can be enhanced. FAC has been used previously in the hierarchical classification of the information in a series of pre- and post-edge EELS images
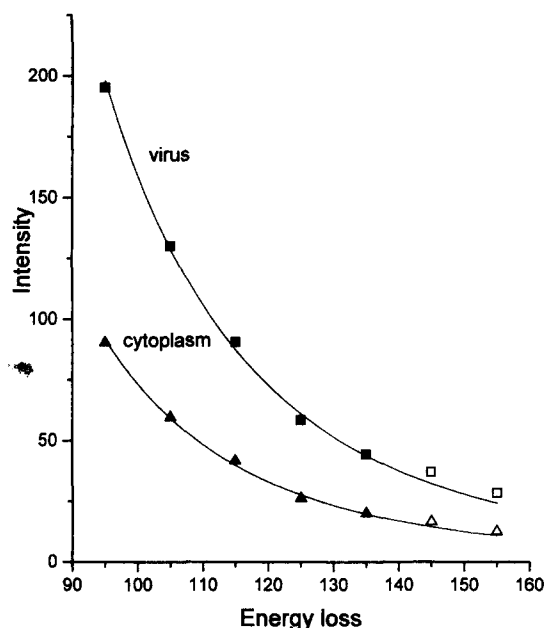
Fig. 7. Plots of average counts versus energy loss values in different regions of interest (ROIs) of the TGEV-containing series. Continuous line represent the adjusted background curve calculated using the pre-edge images (before 145 eV). Data in virus at 145 and 155 eV are over the background curve, indicating the presence of P.

(Trebbia and Mory, 1990), as well as in other types of image analysis (Bretaudiere and Frank, 1986). In our case, FAC has proved to be a successful tool for filtering.

Reconstitution of images has been performed preserving only useful information (characteristic signal and background) that can be present in one factorial axis (series 1 and 2, containing approximately 70% of the global variance) or in two axes, as in the case of virus-containing samples (38% of the global variance). The criteria used to select the number of axes for the reconstitution process were based on the study of the factorial images. Only axes corresponding to those factorial images possessing "organized information" (Bonnet and Trebbia, 1992) should be used for reconstitution. Noise reduction and suppression of acquisition artifacts is thus achieved and consequently, an important increment of the SNR in the filtered P-maps.

Once we tested our system for P-map production, we then tried to use this method for the detection of nucleic acids in intracellular viruses. In our studies, considerable care has been taken with specimen preparation, since in a previous work from our group the structural preservation provided by freeze-substitution has been decisive to characterize the two types of viral-related particles that assemble in coronavirus-infected cells (Risco *et al.*, 1998). In this extended structural work, it was demonstrated that two types of TGEV virions accumulate in infected cells: large viral particles (size of the viral core around 68–80 nm) exhibit an internal clear centre and dense periphery, while small virions (size of the viral core around 50–65 nm) are homogeneously dense inside. To define whether these differences in density are due to different arrangements of the viral RNA, a suitable method for mapping nucleic acids is needed. Encapsidation of the viral genome is one of the most difficult steps to characterize when studying the sequence of viral assembly at the structural level, since RNA is usually detected with methods

of variable efficiency. Only a small percentage of sectioned viral particles react with the probes used in in situ hybridization (ISH) or with RNase-colloidal gold complexes (Risco *et al.*, 1998). An additional problem of ISH is that the simultaneous detection of protein cannot be achieved in most cases, since proteolysis is often necessary to unmask nucleic acid molecules, frequently complexed with viral proteins within the virion. P-maps obtained on sections provide direct information of the RNA distribution, in spite of the presence of proteins complexed with viral proteins within the virion. Our results show two different distributions of phosphorus (and, hence, of RNA) in the viral particles analysed: peripheral (larger virions) or central (smaller virions) arrangement. According to the data obtained in our previous structural study, the small virions are the final product of assembly (infectious mature virions), while the large viral particles most likely represent a precursor form that assembles at early steps in morphogenesis. P-maps indicate, then, that a major change in RNA organization inside the viral particle takes place during the structural maturation suffered by TGEV virions during morphogenesis.

The results presented here show that mapping nucleic acids in viruses is a biological problem that EFTEM can address, providing useful information on viral structure and morphogenesis. These results open up the possibility for further studies to follow the different steps involved in the RNA incorporation into viral particles during morphogenesis and the maturation processes involved. It is also clear that future improvements would demand an increment of the P detection sensitivity by enhancement of the SNR. We are presently carrying out several studies that could be useful to this end, such as the increment in the number of acquired images in the 105–155 eV range of energy loss, and the testing of other background models different from the Egerton power law.

REFERENCES

Adamson-Sharpe K.M., Ottensmeyer F.P., 1981. Spatial resolution and detection sensitivity in microanalysis by electron energy loss selected imaging. *J. Microsc.*, **122**, 309–314.

Abolhassani-Dadras S., Vazquez-Nin G.H., Echevarria O.M., Boutinard Rouelle-Rossier V., Fakan S., 1994. ESI in situ analysis of extrachromosomal RNP granules. *J. Microsc.*, **174**, 23–238.

Abolhassani-Dadras S., Vazquez-Nin G.H., Echevarria O.M., Fakan S., 1996. Image-EELS for in situ estimation of phosphorus content of RNP granules. *J. Microsc.*, **183**, 215–222.

Bazett-Jones D.P., Ottensmeyer F.P., 1981. Phosphorus distribution in the nucleosome. *Science*, **211**, 169–170.

Bazett-Jones D.P., 1993. Empirical basis for phosphorus mapping and structure determination of DNA: protein complexes by electron spectroscopic imaging. *Microbeam Anal. J.*, **2**, 69–79.

Beniac D.R., Czarnota G.J., Rutherford B.L., Ottensmeyer F.P., Harauz G., 1997a. Three-dimensional architecture of Thermomyces lanuginosus small subunit ribosomal RNA. *Micron*, **28**, 13–20.

Beniac D.R., Czarnota G.J., Rutherford B.L., Ottensmeyer F.P., Harauz G., 1997b. The in situ architecture of E. coli ribosomal RNA derived from

electron spectroscopic imaging and three-dimensional reconstruction. *J. Microsc.,* **188,** 24–35.

electron spectroscopic imaging of ribonucleoproteins: correlation of stain and phosphorus. *Biol. Cell,* **87,** 143–147.

High resistivity (up to 10^9 $\Omega \cdot$ cm) cadmium

989.

---

sing image sequences for elemental mapping. *Scanning Microsc. Suppl.,* **2,** 351–364.

Bonnet N., Simova E., Lebonvallet S., Kaplan X., 1992. New applications of multivariate statistical analysis in spectroscopy and microscopy. *Ultramicroscopy,* **40,** 1–11.

Bonnet N., Trebbia P., 1992. Multi-dimensional data analysis and processing in electron-induced microanalysis. *Scanning Microscopy Suppl.,* **6,** 163–177.

Bonnet N., 1995. Processing of images and image series: a tutorial review for chemical microanalysis. *Mikrochim. Acta,* **120,** 195–210.

Bonnet, N. and Zahm, J.M., 1998. Analysis of image sequences in fluorescence videomicroscopy of stationary objects. *Cytometry* **31,** 217–228.

Bretaudiere J.P., Frank J., 1986. Reconstitution of molecular images analyzed by correspondence analysis: a tool for structural interpretation. *J. Microsc.,* **144,** 1–14.

Colliex, C., Tence, M., Lefévre, E., Mory, C., Gu, H., Bouchet, D., Jean-guillaume, C. (1994) Electron Energy Loss Spectrometry mapping. *Mikrochim. Acta* **114/115,** 71-87.

Egerton R.F., 1975. Inelastic scattering of 80 keV electrons in amorphous carbon. *Phil. Mag.,* **31,** 199–215.

Le Furgey A., Davilla S.D., Kopf D.A., Sommer J.R., Ingram P., 1992. Real-time quantitative elemental analysis and mapping: microchemical imaging in cell physiology. *J. of Microsc.,* **165,** 191–223.

Grief C., Nermut M.V., Hockley D.J., 1994. A morphological and immunolabeling study of freeze-substituted human and simian immunodeficiency viruses. *Micron,* **25,** 119–128.

Harauz G., Ottensmeyer F.P., 1984. Nucleosome reconstitution via Phosphorus mapping. *Science,* **226,** 936–940.

Harauz G., Evans D.H., Beniac D.R., Arsenault A.L., Rutherford B., Ottensmeyer F.P., 1995. Electron spectroscopic imaging of encapsidated DNA in vaccinia virus. *Can. J. Microbiol.,* **41,** 889–894.

Hofer F., Warbichler P., Grogger W., 1995. Imaging of nanometer-sized precipitates in solids by electron spectroscopic imaging. *Ultramicroscopy,* **59,** 15–31.

Heng Y.-M., Simon G.T., Boublik M., Ottensmeyer F.P., 1990. Experimental ionization cross-sections of phophorus and calcium by electron spectroscopic imaging. *J. Microsc.,* **160,** 161–171.

Jeanguillaume C., Colliex C., Trebbia P., 1978. About the use of electron energy loss spectroscopy for chemical mapping of thin foils with high spacial resolution. *Ultramicroscopy,* **3,** 137–142.

Korn A.P., Spitnik-Elson P., Elson D., Ottensmeyer F.P., 1983. Specific visualization of ribosomal RNA in the intact ribosome by electron spectroscopic imaging. *Eur. J. Cell Biol.,* **31,** 334–340.

Krivanek O.L., Alexander J.G., Dellby N., Meyer C.E., 1992. Design and first applications of a post-column imaging filter. *Microsc. Microanal. Microsctruct.,* **3,** 187–199.

Krivanek O.L., Friedman S.L., Gubbens A.J., Kraus B., 1995a. An imaging filter for biological applications. *Ultramicroscopy,* **59,** 267–282.

Krivanek O.L., Kundmann M.K., Kimoto K., 1995b. Spatial resolution in EFTEM elemental maps. *J. Microsc.,* **180,** 277–287.

Leapman R.D., 1986. Scanning transmission electron microscope (STEM) elemental mapping by electron energy loss spectroscopy. *Annals New York Acad. Sci.,* **483,** 327–338.

Leapman R.D., Hunt J.A., 1991. Comparison of detection limits for EELS and EDXS. *Microsc. Microanal. Microstruct.,* **2,** 231–244.

Olins A.L., Olins D.E., Bazett-Jones D.P., 1996. Osmium ammine-B and

limitations, compromises. *Annals New York Acad. Sci.,* **483,** 339–353.

Ottensmeyer F.P., Andrew J.W., 1980. High-resolution microanalysis of biological specimens by electron energy loss spectroscopy and by electron spectroscopic imaging. *J. Ultrastruct. Res.,* **72,** 336–348.

Ottensmeyer F.P., Frankland B.W., 1988. Spectral processing for parallel recording of elemental maps. *Scanning Microsc. Suppl.,* **2,** 343–350.

Ottensmeyer F.P., Andrews A.L., Arsenault Y.M., Heng G.T., Simon G.C., Weatherly G.C., 1988. Elemental Imaging by Electron Energy Loss Microscopy. *Scanning,* **10,** 227–238.

Özel M., Pauli G., Gelderblom H.R., 1990. Electron spectroscopic imaging (ESI) of viruses using thin-section and immunolabeling preparations. *Ultramicroscopy,* **32,** 35–41.

Quintana C., 1991. X-ray microanalysis of cell nuclei. *J. Electron Microsc. Techn.,* **18,** 411–423.

Quintana C., 1994. Cryofixation, cryosubstitution, cryoembedding for ultrastructural, immunocytochemical and microanalytical studies. *Micron,* **25,** 63–99.

Quintana C., Bonnet N., 1994a. Improvements in biological X-ray microanalysis: cryoembedding for specimen preparation and multivariate statistical analysis for data interpretation. *Scanning Microsc. Suppl.,* **8,** 83–99.

Quintana C., Bonnet N., 1994b. Multivariate statistical analysis applied to X-ray spectra and X-ray mapping of liver cell nuclei. *Scanning Microsc.,* **8,** 563–586.

Quintana C., Marco S., Carrascosa J.L., 1997. Evaluation of the analytical and imaging performances of a non-dedicated TEM equipped with a parallel electron energy loss spectrometer (PEELS) and image filter (IF). *J. Trace Microprobe Techn.,* **15,** 175–188.

Rattner J.B., Bazett-Jones D.P., 1989. Kinetochore structure: electron spectroscopic imaging of the kinetochore. *J. Cell Biol.,* **108,** 1209–1219.

Reimer L., Messemer W.M.R., 1990. Contrast in the electron spectroscopic imaging mode of a TEM. II. Z-ratio, structure-sensitive and phase contrast. *J. Microsc.,* **159,** 143–160.

Risco C., Antón I.M., Suñé C., Pedregosa A.M., Martín-Alonso J.M., Parra F., Carrascosa J.L., Enjuanes L., 1995. Membrane protein molecules of transmissible gastroenteritis coronavirus also expose the carboxy-terminal region on the external surface of the virion. *J. Virol.,* **69,** 5269–5277.

Risco C., Muntión M., Enjuanes L., and Carrascosa J.L. (1998) Two types of viral-related particles are found during TGEV morphogenesis. J. Virol., **12,** 4022–4031.

Tenailleau H., Martin J.M., 1992. A new background subtraction for low-energy EELS core edges. *J. of Microsc.,* **166,** 297–306.

Shuman H., Chang C.F., Buhle J.R., Somlyo A.P., 1986. Electron Energy Spectroscopy: Quantitation and Imaging. *Annals New York Acad. Sci.,* **483,** 295–310.

Trebbia P., Bonnet N., 1990. EELS elemental mapping with unconventional methods. I. Theoretical basis: image analysis with multivariate statistics and entropy concepts. *Ultramicroscopy,* **34,** 165–178.

Trebbia P., Mory C., 1990. EELS elemental mapping with unconventional methods. II. Applications to biological specimens. *Ultramicroscopy,* **34,** 179–203.

Vazquez-Nin G.H., Abolhassani-Dadras S., Echevarria O.M., Boutinard Rouelle-Rossier V., Fakan S., 1996. Phosphorus distribution in peri-chromatin granules and surrounding nucleoplasm as visualized by electron spectroscopic imaging. *Biol. Cell,* **87,** 171–177